A Numerical Study on the Influence of Confining Walls on Drag and Heat Transfer Coefficients in Single-Particle Lab-Scale Reactors

Philipp Reinold*, Martin Kutscherauer and Gregor D. Wehinger

Dedicated to Prof. Dr.-Ing. Andreas Seidel-Morgenstern on the occasion of his retirement

Supporting Information
available online

Single-particle reactors in lab-scale are a promising technology to gain an in-depth understanding of the intricate reaction and transport processes that occur in catalyst particles under operando conditions. It is not described whether the effect of the bounding walls in such narrow flow channels influence the processes at the particle. Therefore, this work applies three-dimensional (3D) computational fluid dynamics (CFD) simulations to analyze the drag coefficient C_D alongside the local and average particle Nusselt number Nu_p as characteristic local and integral quantities in the range of particle Reynolds numbers $10 \leq Re_p \leq 10^3$. An equation is derived to correct for the wall effects on C_D and Nu_p and assist the experimenter in the interpretation of measured results.

Keywords: Computational fluid dynamics, Drag coefficient, Heat transfer, Single-particle reactor, Wall effects

1 Introduction

In a novel class of lab-scale reactors operando measurement techniques are applied to heterogeneous catalytic reactors, in which a moving capillary resolves spatial concentration and temperature profiles. Their application has been demonstrated across various reactor types, e.g., inside honeycomb monoliths [1, 2], catalytic foams [3, 4], fixed-bed reactors [5, 6], and recently inside a single catalytic pellet [7]. The latter case aims to resolve intraparticle gradients and the surrounding boundary layer. However, even this method is invasive, but its effect on the physical-chemical behavior of the particle is not yet quantified. Intraparticle processes are driven by the conditions the external flow applies and, thus, influences hereon an important aspect.

The drag force and heat transfer of single particles have been widely studied in literature particularly for spheres that are falling into a tube or held stationary in a stream, as described in the relevant literature [8]. In a recent review, Michaelides and Feng [9] compile the current understanding on drag coefficients for non-spherical particles and present several correlations from literature. Among their gathered expressions is the work from Haider and Levenspiel [10], who derive a generalized formulation for spherical and non-spherical particle shapes based on the sphericity.

Ganser [11] proposes a modified expression with two shape factors that also includes the size of the settling tube. A more sophisticated correlation by Hölzer and Sommerfeld [12] is based on the sphericity and two additional sphericity factors that depend on the particle´s orientation.

The effect of confining walls on particle hydrodynamics has previously been studied, as summarized in [13], and can be described by a drag correction factor. However, the majority of investigations are focused on spheres in the creeping flow regime ($Re_p \ll 1$, $Re_p = u\rho d_p/\mu$) bounded by a cylindrical tube [14, 15], with some works taking into account differently shaped enclosing boundaries [16, 17]. Catalytic particles are, however, most often differently shaped for optimal performance of fixed-bed reactors which is why these correction factors are of limited use.

The heat transfer of particles and cylinders under forced convection has been widely investigated resulting in

[1]Philipp Reinold https://orcid.org/0009-0004-2854-0145
(philipp.reinold@kit.edu), [1]Martin Kutscherauer
 https://orcid.org/0000-0002-1892-2033,
[1]Prof. Gregor D. Wehinger
 https://orcid.org/0000-0002-1774-3391
[1]Karlsruhe Institute of Technology, Institute of Chemical Process Engineering, Kaiserstr. 12, 76131 Karlsruhe, Germany.
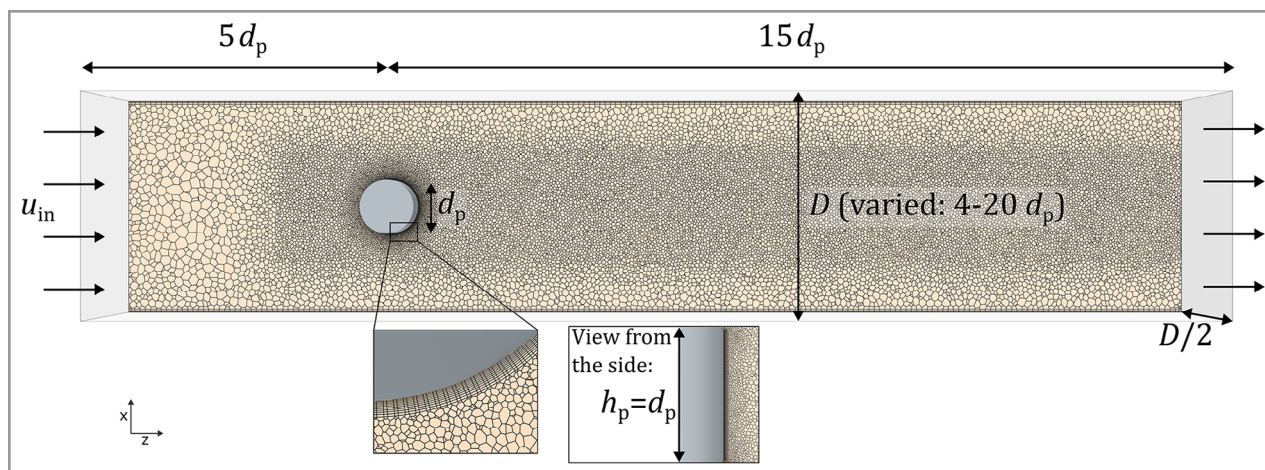
Figure 1. Geometry setup and plane section through the mesh of the single-particle reactor (see nomenclature for description details; $d_p = 5$ mm).

numerous correlations, of which the Nusselt correlation by Whitaker [18] for spherical particles and the correlations by Gnielinski [19] and Sparrow [20] for cylinders are to be mentioned. Most of the published research on heat transfer from cylinders focuses on infinitely elongated cylinders due to the relevance for convective heat transfer from tubes and in multitubular heat exchangers. While this flow is characterized by a two-dimensional structure, the flow around a finite cylinder is more complex and three-dimensional as described in detail by Zdravkovich [21].

Several studies on the flow around single particles exist in literature using computational fluid dynamics (CFD). Dhole [22] studied the heat transfer from spheres in unconfined flow for different thermal boundary conditions in the range of $5 \leq Re_p \leq 200$. Dixon [23] scrutinized flow and heat transfer for a single sphere focusing on the mesh development for fixed-bed reactors, where $Re_p \geq 400$. In a later work, Dixon [24] examined how the inclination angle affects reaction and transport in a ring-shaped catalyst for $10^3 \leq Re_p \leq 10^4$. However, there is a lack of studies that investigate the conditions relevant to single-particle lab-scale reactors, where Re_p lies between 10 and 10^3 and reactor walls are in proximity.

This study aims to provide a detailed view on the external flow field and investigate how the flow around and heat transfer at the surface of a cylindrical particle is influenced by the confining walls. Therefore, the CFD simulations focus on a single particle within the channel without any further fittings. The shape and dimensions of the particle and flow channel are chosen based on a single-particle profile reactor described in literature [7]. The impact of the confining walls on fluid flow and heat transfer is quantified by comparing characteristic local and integral quantities, namely, the drag coefficient together with the local and average particle Nusselt numbers. Based on a parameter variation across the CFD simulations an equation is derived to correct for the

influence of confining walls on drag coefficient and particle Nusselt number.

2 Theory and Methods

The simulations are conducted using the commercial CFD software Siemens Simcenter STAR-CCM+ version 18.02.010-R8. Descriptions of the governing equations for the laminar flow simulations and the applied turbulence model are covered by Sect. 2.2. Sect. 2.3 elaborates on the geometry and mesh settings, alongside a precedent grid convergence study.

To assess the magnitude of possible wall effects in lab-scale reactors, an example from literature is taken as a reference case, as shown in Fig. 1, where a single cylindrical particle is placed in a rectangular channel and mounted on a platform [7]. To exclude any effects exhibited by either the platform or the capillary itself, the simulation geometry of this study contains only the particle. The simulations follow a series of parameter variations. Inlet velocities are varied therein based on particle Reynolds numbers of 10, 100, and 1000, as defined by Eq. (1). Additionally, the channel size D, i.e., width and height, is varied between 4 d_p and 20 d_p, with d_p being the particle diameter. In total, the study spans 15 simulations. Three additional simulations are carried out at a width of 20 d_p, all with a symmetry boundary condition, i.e., the velocity gradient normal to the wall is set to zero, in order to reflect the unbounded flow condition around the cylinder.

2.1 Dimensionless Numbers

The particle Reynolds number is defined as:

$$Re_p = \frac{u_{in} \rho_f d_p}{\mu} \tag{1}$$

Here, u_{in} is the inlet velocity, ρ_f is the fluid density, and μ denotes the dynamic viscosity. Several dimensionless quantities are utilized to evaluate the effects of confining walls. The drag coefficient C_D is calculated as follows:

$$C_D = \frac{F_z}{\frac{1}{2}\rho_f u_{in}^2 A_{proj}} \tag{2}$$

where F_z represents the drag force and A_{proj} is the surface area of the particle projected in the incident flow direction. As a characteristic quantity of the heat transfer, the local Nusselt number is determined by the equation:

$$Nu_{loc} = \frac{\alpha_{loc} d_p}{\lambda_f} \tag{3}$$

where the local heat transfer coefficient α_{loc} is derived by Eq. (4) from the surface heat flux $\dot{q}_s$ and the difference between the surface temperature T_s and a reference temperature T_{in}, which is in this study the inlet temperature.

$$\alpha_{loc} = \frac{\dot{q}_s}{T_s - T_{in}} \tag{4}$$

The average particle Nusselt number Nu_p can be obtained by:

$$Nu_p = \frac{1}{A_p}\int_0^{A_p} Nu_{loc} dA \tag{5}$$

The Lewis number Le relates the thermal boundary layer thickness to the concentration boundary layer thickness and is defined as:

$$Le = \frac{Sc}{Pr} = \frac{\lambda_f}{D_f c_p \rho_f} \tag{6}$$

where Sc is the Schmidt number, Pr is the Prandtl number, and D_f is the diffusion coefficient. The velocity field and local Nusselt number along the curved cylinder surface are further aspects that are subjected to comparison and subsequent discussion.

2.2 Governing Equations

The following set of partial differential equations describe the present case of a non-reactive fluid system at steady state with heat transfer from a hot particle surface to the bulk fluid. In an infinitesimal control volume, the conservation of mass reads:

$$\frac{\partial(\rho_f u_i)}{\partial x_i} = 0 \tag{7}$$

The conservation of momentum is given by:

$$\frac{\partial(\rho_f u_i u_j)}{\partial x_j} = -\frac{\partial p}{\partial x_i} + \frac{\partial \tau_{ij}}{\partial x_j} \tag{8}$$

where p is the static pressure and τ_{ij} denotes the stress tensor. For a Newtonian fluid, the stress tensor τ_{ij} is written as:

$$\tau_{ij} = \left[\mu\left(\frac{\partial u_i}{\partial x_j} + \frac{\partial u_j}{\partial x_i}\right)\right] - \frac{2}{3}\mu\frac{\partial u_k}{\partial x_k}\delta_{ij} \tag{9}$$

The energy balance in terms of specific enthalpy h is expressed as:

$$\frac{\partial(\rho_f h u_i)}{\partial x_i} = \tau_{ij}\frac{\partial u_i}{\partial x_j} + \frac{\partial}{\partial x_i}\left(\lambda_f\frac{\partial T}{\partial x_i}\right) \tag{10}$$

While this system of partial differential equations applies to laminar flows for the cases $Re_p = 10$ and 100, the turbulent flow simulations are modeled by the Reynolds-averaged Navier-Stokes (RANS) equations in the case of $Re_p = 1000$. The additional Reynolds stress tensor, resulted from averaging the solution variables, is modeled by applying the Boussinesq hypothesis. The variations of available RANS models are described extensively in standard literature [25]. In this work, the realizable k-ε model with a two-layer all-y^+ wall treatment driven by shear is used; see details in [26, 27].

2.3 Computational Domain and Meshing

The exemplary single-particle reactor from [7] consists of an equilateral, cylindrical particle, with $d_p = 5$ mm, placed in a rectangular channel with a height of 4 d_p, a width of 4 d_p, and a total length of 12 d_p. In the simulations, the distance to the inlet and outlet is chosen to be larger than this to ensure that the computation is not affected by these boundaries. Dixon [23] has demonstrated that for a sphere across a wide range of Re_p, distances of 5 d_p and 15 d_p from the particle to the inlet and outlet, respectively, are sufficient and hence are employed in the present investigation. The setup for the simulations is illustrated in Fig. 1 alongside a plane cutting through the mesh.

The mesh settings for all domains comprise a base cell size of $d_p/10$ along with refinements in the wake and at the particle surface of $d_p/20$ and $d_p/100$, respectively. Prism layers are generated at the particle surface and consist of ten layers with a stretching factor of 1.1. As proposed by Dhole [22], the prism layer total thickness is approximated by the momentum boundary layer thickness δ_m at the highest investigated Re_p, which is derived from Schlichting [28] in Eq. (11). The momentum and thermal boundary layers are described by Eqs. (11) and (12), respectively [22].

$$\delta_m = 1.13 d_p Re_p^{-0.5} \tag{11}$$

$$\delta_t = \delta_m Pr^{-1/3} \tag{12}$$

Here, δ_t represents the thickness of the thermal boundary layer. The meshing procedure includes a grid independence study, following the grid convergence index approach as described by Roache [29]. The estimation of the error E is obtained through Richardson extrapolation using Eq. (15) by extrapolating the solution variable Φ from a medium resolved (m) and fine (f) mesh. A refinement factor r_g is

calculated from the cell count N and a convergence rate of $p = 2$ is assumed [30].

$$r_g = \sqrt{\frac{N_f}{N_m}} \qquad (13)$$

$$\Phi_\infty = \Phi_f + \frac{\Phi_f - \Phi_m}{r_g^p - 1} \qquad (14)$$

$$E = \left| \frac{\Phi_\infty - \Phi_f}{\Phi_\infty} \right| \qquad (15)$$

These meshes are simulated at a Reynolds number of 1000 resulting in a Richardson error for each variable, drag coefficient C_D, and Nusselt number Nu_p. This error is compared among a coarse, medium, and fine mesh to determine the solution's grid independency.

2.4 Boundary Conditions

A no-slip condition is imposed on the confining wall and particle surface boundaries. The inlet fluid velocity is specified based on the respective Reynolds number. The outlet pressure is set to ambient pressure. The confining walls are assumed to be adiabatic, whereas the surface temperature T_s of the particle remains constant at $\Delta T = T_s - T_{in} = 30$ K. Additional simulations apply a symmetry boundary condition at the confining wall, which sets the velocity gradient normal to the wall to zero. These simulations are used to replicate an infinitely large channel excluded from any wall effects.

Fluid properties are set to constant values and taken from a single particle study from literature [23], with a density ρ_f of 6.1616 kg m^{-3}, heat capacity c_p of 2395.38 J kg^{-1} K^{-1}, dynamic viscosity μ of $3.0 \cdot 10^{-5}$ Pa s, and thermal conductivity λ_f of 0.0876 W m^{-1} K^{-1}. This corresponds to a typical reactive gas mixture under pressure [23]. Assuming a Lewis number of $Le \gg 1$, the concentration boundary layer thickness around the particle becomes thinner and is therefore less influenced by the confining walls compared to the thermal boundary layer. Thus, species transport is excluded for the remainder of the study.

3 Results and Discussion

The results of the mesh independency study can be found in Sect. S1 of the Supporting Information (SI). The final mesh settings are used throughout all simulations. Additionally, the assumption of a steady-state flow regime is verified for $Re_p = 100$ as well as for the RANS model at $Re_p = 1000$ and can be found in the SI in Sect. S3.

3.1 Velocity Profiles

Narrow flow channels have a significant impact on the velocity field. Fig. 2 displays the velocity magnitude $|u|$ and fluid temperature with isolines at $Re_p = 10$ in a cross section located centrally in the x-z plane (see also Fig. 1) for domain sizes of 4 d_p, 12 d_p and 20 d_p from top to bottom. The flow direction is from left to right. Qualitative differences are clearly visible, particularly the vena contracta at $D = 4\ d_p$, i.e., the flow acceleration (by approx. factor 2) caused by the narrow gap between particle surface and wall. The effect is not limited to the far-field but rather impacts the flow at the vicinity of the particle's surface, which is perceivable in the forward stagnation zone and wake region for both velocity and temperature.

Discrete velocity values are extracted along the line probes, highlighted in Fig. 2, and plotted in Fig. 3 as velocity profiles normalized by the respective inlet velocity u_{in}. The profiles are shown for all investigated sizes and Re_p of 10, 100, and 1000 in Figs. 3a, 3b, and 3c, respectively.

Additional simulations with a symmetry boundary, denoted as ∞, reflect the case of an infinitely large domain size without any wall effects. The velocity profile is generally more affected at lower Re_p, where viscous forces dominate and cause a thicker boundary layer. It is noteworthy that even the largest domain size (20 d_p) influences the velocity profile around the particle for $Re_p = 10$, as one can observe a deviation from the simulations with symmetry boundary (∞).

The relative velocity increase in Fig. 3a appears to grow nonlinearly with decreasing channel width. At $Re_p = 10$ the smallest channel size results in a maximum velocity increase to 1.86 u_{in}, while this value reduces to 1.31 u_{in} at $Re_p = 1000$. The diversely shaped profiles between D suggest that the gradients at the particle surface differ. Consequently, the wall shear rate and heat transfer are locally affected. Fig. S4 provides a visualization of the wall shear rate at the particle surface for the cases shown in Fig. 2.

3.2 Drag Coefficient

As the cylinder is exposed to a fluid stream, it is subjected to a drag force. The corresponding drag coefficient C_D is calculated by Eq. (2) and plotted against Re_p for each channel size of the study in Fig. 4a. The ratio to the value obtained with symmetry boundary $C_D/C_{D,\infty}$ serves as a measure of deviation from ideality and is plotted in Fig. 4b against the normalized channel width D/d_p. As observed in the velocity profile, reducing the channel width to 4 d_p results in the highest deviation. At low Re_p, the C_D yields 11.69, while a symmetry boundary deviates by approx. 162 % given a C_D of 4.46. As Re_p and D/d_p increase, the deviations gradually decrease. However, differences persist at the largest domain size (20 d_p) of up to 10 % for $Re_p = 10$.

A nonlinear least squares fit on the CFD data yields the following expression to describe the wall effects in the present work:

$$C_D/C_{D,\infty} = 1 + \beta_0 \exp\left(-\beta_1 \left(D/d_p\right)\right) Re_p^{\beta_2} \qquad (16)$$
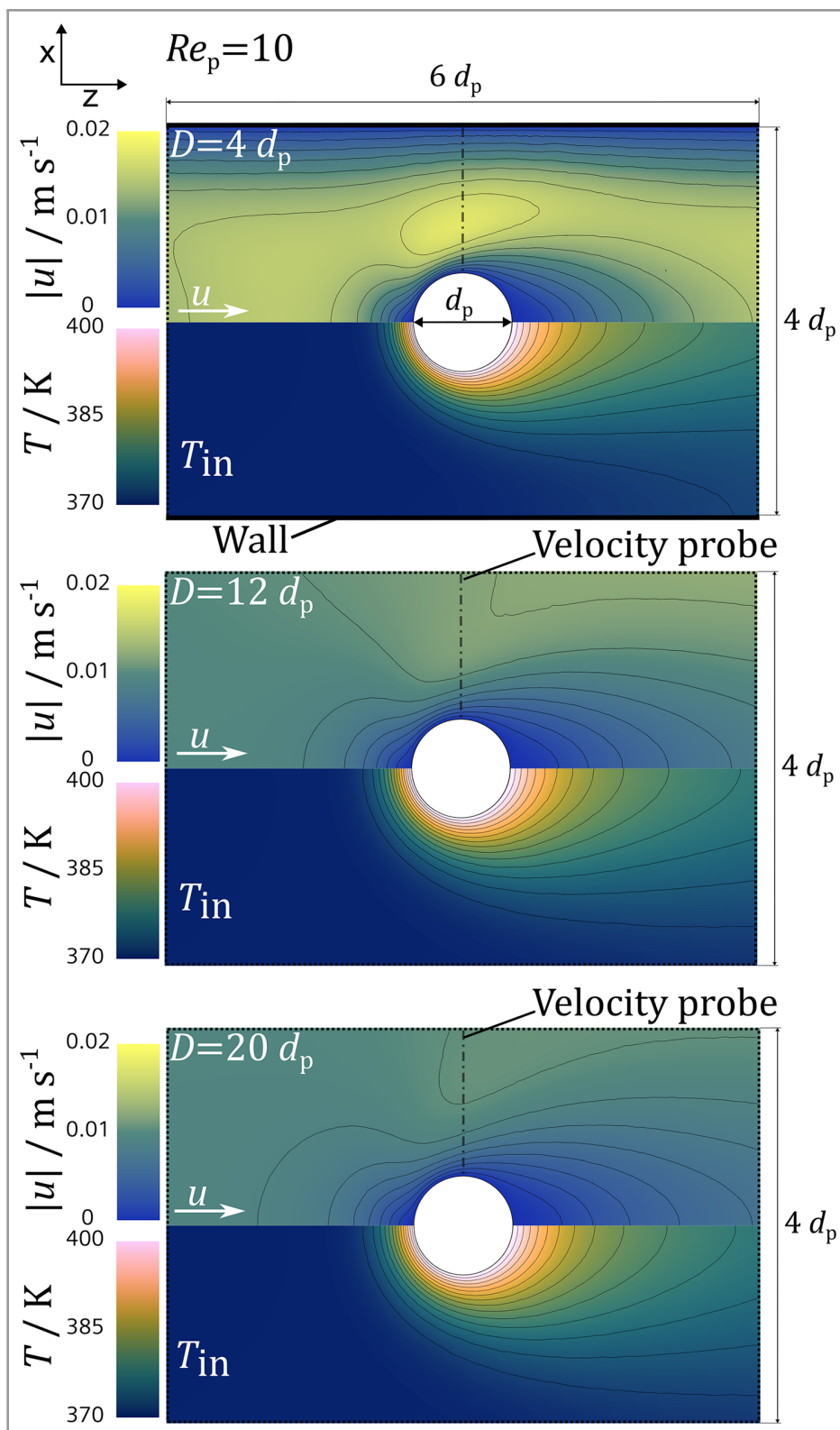
Figure 2. Velocity and temperature fields in centrally placed *x-z* plane sections around the particle at $Re_p = 10$ and channel sizes of 4 d_p (top), 12 d_p (middle), and 20 d_p (bottom), and velocity probe (dash-dotted). Flow is from left to right.
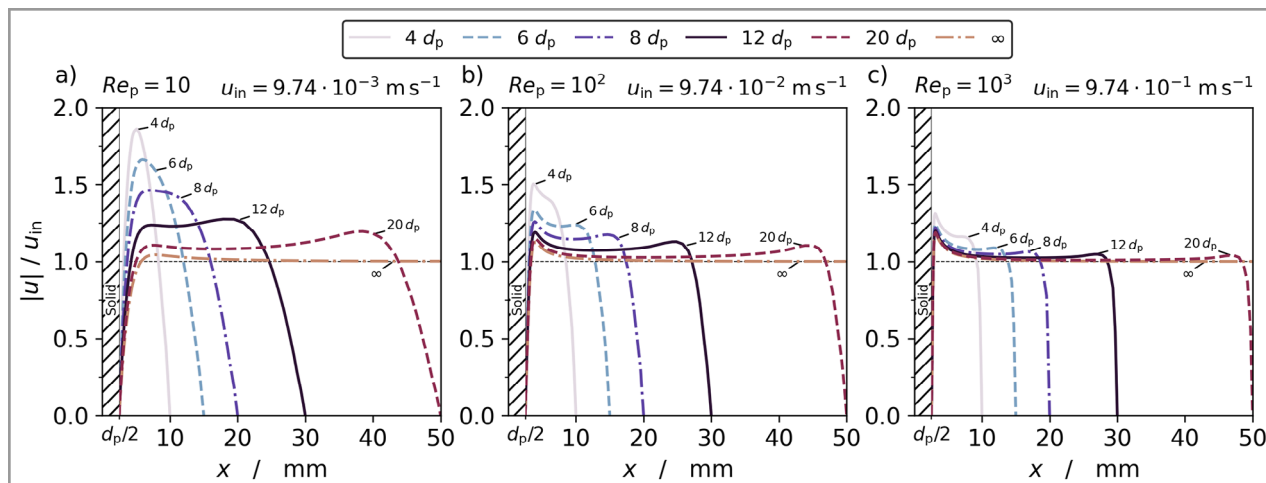
Figure 3. Normalized velocity magnitude in the cross section between particle and wall for various channel widths at Re_p of a) 10, b) 100, and c) 1000.

with fitted coefficients of $\beta_0 = 9.79$, $\beta_1 = 0.23$, $\beta_2 = -0.39$, and a root mean squared error of RMSE $= 3.223 \cdot 10^{-2}$. A comparison of the mean and maximum deviation to the CFD data is provided for the presented equation and a literature correlation in Tab. S2.

3.3 Particle Nusselt Number

The particle Nusselt number is obtained by averaging the local Nusselt number over the cylinder surface, using Eq. (5). As outlined in Sect. 3.1, an increase in Nu_p is expected due to the confinement with the largest deviations observed at $Re_p = 10$. Fig. 5a shows Nu_p plotted against Re_p for each channel size considered, while Fig. 5b depicts the ratio $Nu_p/Nu_{p,\infty}$ similar to the considerations made in Sect. 3.2 for the drag coefficient. The deviation is less pronounced than for the drag, but a notable systematic error is introduced, especially at low Re_p, if the wall effects were neglected. The expression to describe this effect is of the same form as in the previous section and reads:

$$Nu_p/Nu_{p,\infty} = 1 + \beta_0 \exp\left(-\beta_1 \left(D/d_p\right)\right) Re_p^{\beta_2} \tag{17}$$

A nonlinear least squares fit yields $\beta_0 = 0.89$, $\beta_1 = 0.19$, and $\beta_2 = -0.28$ with RMSE $= 6.823 \cdot 10^{-3}$.

It must be noted that the use of the suggested wall corrections in Eqs. (16) and (17) is limited to Newtonian fluids in the particular Re_p range and the particle shape considered in this work. Moreover, influences by the Pr number are not included. Thus, they are not a generalized correlation to represent a wide array of cases.

3.4 Local Nusselt Number

The local Nusselt number, as calculated from Eq. (3), is determined on a circular line along the cylinder surface

from the forward stagnation point to the rear stagnation point. These values are plotted in Fig. 6 against the angle θ to the forward stagnation point. Nu_{loc} is displayed for each investigated size at $Re_p = 10$ (Fig. 6a), 100 (Fig. 6b), and 1000 (Fig. 6c). The largest relative deviations from the infinite domain (∞) are observed at the forward stagnation point ($\theta = 0°$), particularly at $Re_p = 10$. At this particle Reynolds number, the deviations continuously decrease downstream until the rear stagnation point ($\theta = 180°$).

As expected from the distinguished flow conditions in Figs. 6a–c, the curves differ in shape and magnitude and show local minima at the separation point before rising again [21]. Some of the values in Fig. 6c that are located below θ of approx. 65° slightly scatter. This can be attributed to utilizing the RANS turbulence model, which approximates turbulence by time-averaged flow quantities and models the turbulent eddy viscosity. However, a qualitative impression of the curve and the less marked extent of the wall effect is pertained.

4 Conclusions

The present numerical study demonstrates that in the range of $10 \leq Re_p \leq 10^3$ and channel sizes of $4\,d_p$ to $20\,d_p$ the flow and heat transfer of a cylindrical particle underlie effects from the confining walls. As a characteristic quantity, the drag coefficient and particle Nusselt number are used to quantify this wall effect. The deviation to an ideal, unbounded flow can be estimated within the range of the parameter study by the expressions proposed in Eqs. (16) and (17). This approach shows that a thoroughly validated CFD model can assist in deconvoluting wall effects. Further, strong local effects are unraveled by examining Nu_{loc} along the particle side wall and most pronounced at the forward stagnation point. The wall corrections are deemed
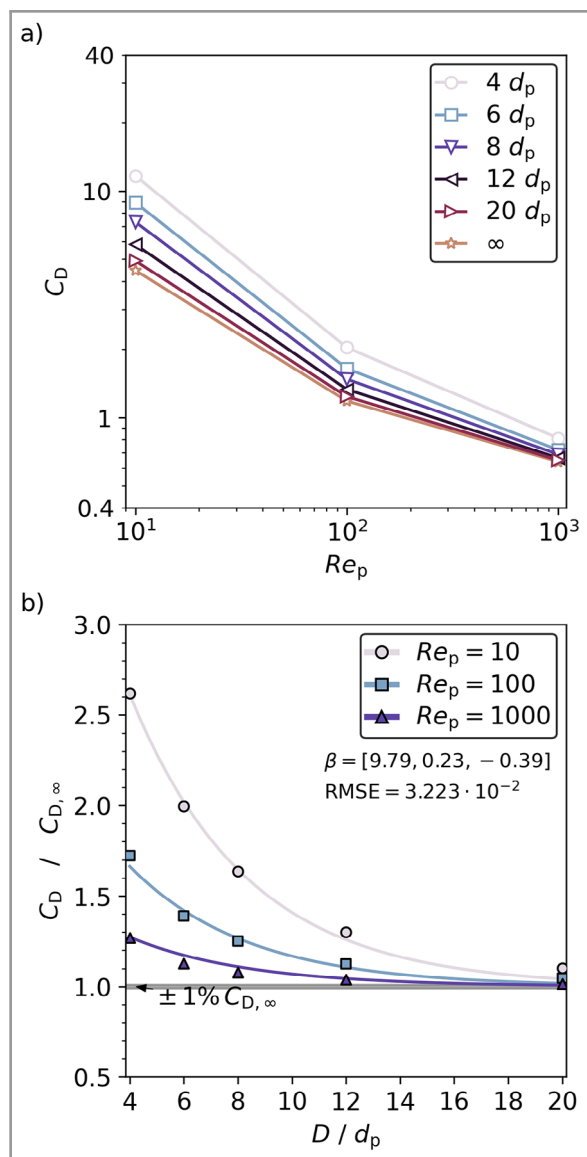
Figure 4. a) C_D over Re_p and b) deviation to infinite domain $C_{D,\infty}$ for varying channel size with wall correction (solid line) from Eq. (16) and CFD data for $Re_p = 10$ (●), 100 (■), and 1000 (▲).

Figure 5. a) Nu_p over Re_p and b) deviation to infinite domain $Nu_{p,\infty}$ for varying channel size with wall correction (solid line) from Eq. (17) and CFD data for $Re_p = 10$ (●), 100 (■), and 1000 (▲).

particularly useful for $Re_p \leq 10^2$, where dominating viscous forces increase the boundary layer thickness and the flow field becomes more influenced by narrow channels.

This work is restrained to cases where the concentration boundary layers are thin compared to the thermal boundary layer $Le \gg 1$. Under this condition, mass transfer is consequently less affected by the walls than heat transfer. In this case it is sufficient to examine solely the heat transfer to assess whether wall effects are present. The influence of the confining walls can significantly affect the catalytic
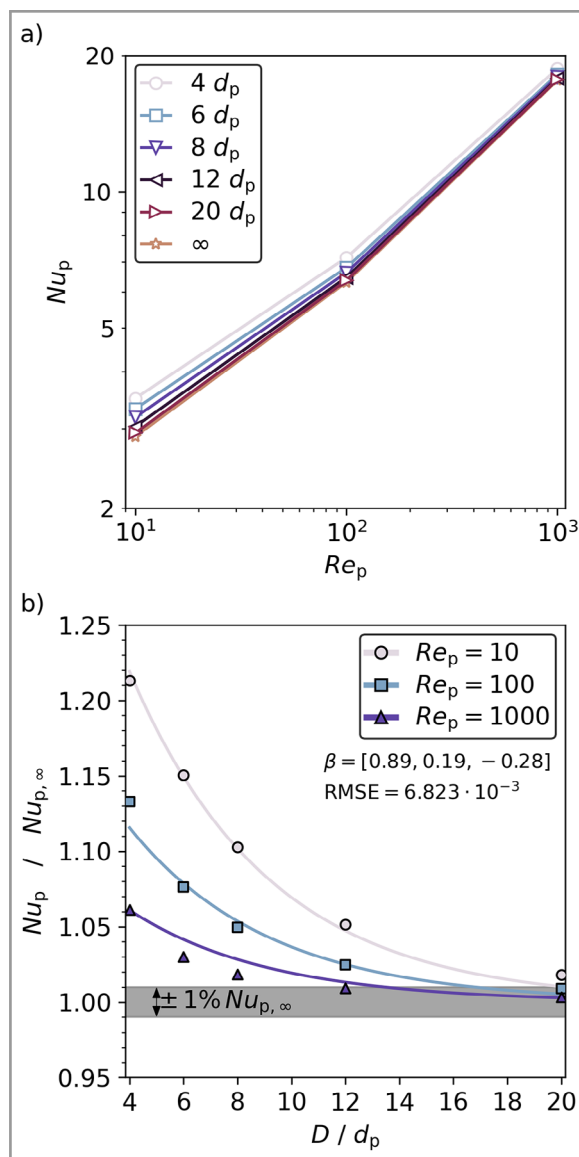
reaction and has to be taken into account when operating a single-particle reactor.

The wall corrections presented in this work should consequently be considered when interpreting experimental results that stem from a setup with limited space capacity, where wall effects on heat and mass transport occur. Further work will include chemical reaction and intraparticle mass transport. Therefore, CFD modeling is suggested as an accompanying part to lab-scale experiments that are performed under reaction conditions.
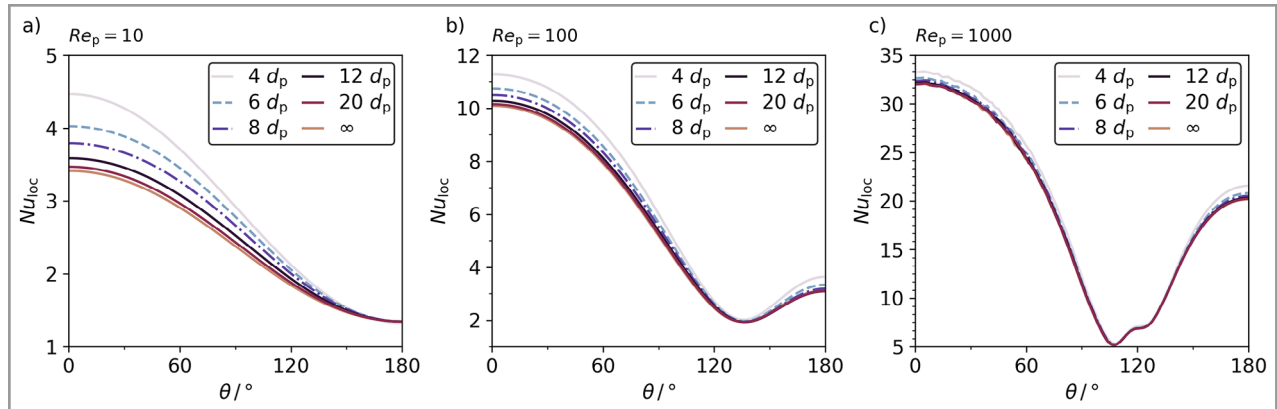
Figure 6. Local Nusselt number along the cylinder side over the angle θ to the forward stagnation point for Re_p of a) 10, b) 100, and c) 1000 at each channel width.

Supporting Information

Supporting information for this article can be found under DOI: https://doi.org/10.1002/cite.202400083.

Acknowledgment

Symbols used

A	[m^2]	area
c_p	[J kg^{-1}K^{-1}]	mass-specific heat capacity
C_D	[–]	drag coefficient
d	[m]	diameter
D	[m]	channel width
D_f	[m^{2}s^{-1}]	diffusion coefficient
E	[–]	Richardson error
F_z	[kg m s^{-2}]	drag force
h	[J kg^{-1}]	mass-specific enthalpy
Le	[–]	Lewis number: $Le = \frac{\lambda_f}{D_f c_p \rho_f}$
Nu_{loc}	[–]	local Nusselt number: $Nu_{loc} = \frac{\alpha_{loc} d_p}{\lambda_f}$
p	[Pa]	pressure
Pr	[–]	Prandtl number: $Pr = \frac{\mu c_p}{\lambda_f}$
$\dot{q}_s$	[W m^{-2}]	surface heat flux
Re_p	[–]	particle Reynolds number: $Re_p = \frac{u_{in} \rho_f d_p}{\mu}$
Sc	[–]	Schmidt number: $Sc = \frac{\mu}{\rho_f D}$
T	[K]	temperature
u	[m s^{-1}]	velocity

Greek letters

α	[W m^{-2}K^{-1}]	heat transfer coefficient
β	[–]	fitting coefficient
δ_{ij}	[–]	Kronecker delta
δ_m	[m]	momentum boundary layer thickness
δ_t	[m]	thermal boundary layer thickness
λ	[W m^{-1}K^{-1}]	thermal conductivity
μ	[kg m^{-1}s^{-1}]	dynamic viscosity
Φ	[a.u.]	solution variable, unit varies
ρ	[kg m^{-3}]	mass density
τ	[N m^{-2}]	stress tensor

Sub- and superscripts

D	drag
f	fluid; fine
in	inlet
loc	local
m	medium
p	particle
proj	projected
s	surface
∞	unbounded flow

Abbreviations

CFD	computational fluid dynamics
RANS	Reynolds-averaged Navier-Stokes
RMSE	root mean squared error

References

[1] M. Hettel, C. Antinori, O. Deutschmann, *Emiss. Control Sci. Technol.* **2016**, *2* (*4*), 188–203. DOI: https://doi.org/10.1007/s40825-016-0043-1

[2] A. M. Gänzler, M. Casapu, D. E. Doronkin, F. Maurer, P. Lott, P. Glatzel, M. Votsmeier, O. Deutschmann, J.-D. Grunwaldt, *J. Phys. Chem. Lett.* **2019**, *10* (*24*), 7698–7705. DOI: https://doi.org/10.1021/acs.jpclett.9b02768

[3] R. Horn, N. J. Degenstein, K. A. Williams, L. D. Schmidt, *Catal. Lett.* **2006**, *110* (*3*), 169–178. DOI: https://doi.org/10.1007/s10562-006-0117-8

[4] R. Horn, O. Korup, M. Geske, U. Zavyalova, I. Oprea, R. Schlögl, *Rev. Sci. Instrum.* **2010**, *81* (*6*), 064102. DOI: https://doi.org/10.1063/1.3428727

[5] G. D. Wehinger, M. Kraume, V. Berg, O. Korup, K. Mette, R. Schlögl, M. Behrens, R. Horn, *AIChE J.* **2016**, *62* (*12*), 4436–4452. DOI: https://doi.org/10.1002/aic.15520

[6] A. B. Shirsath, M. L. Schulte, B. Kreitz, S. Tischer, J.-D. Grunwaldt, O. Deutschmann, *Chem. Eng. J.* **2023**, *469*, 143847. DOI: https://doi.org/10.1016/j.cej.2023.143847

[7] B. Sosna, O. Korup, R. Horn, *J. Catal.* **2020**, *381*, 285–294. DOI: https://doi.org/10.1016/j.jcat.2019.11.005

[8] R. G. Clift, *Bubbles, Drops, and Particles*, 3rd ed., Academic Press, New York **1978**.

[9] E. E. Michaelides, Z. Feng, *J. Fluids Eng.* **2023**, *145* (*6*), 060801. DOI: https://doi.org/10.1115/1.4057019

[10] A. Haider, O. Levenspiel, *Powder Technol.* **1989**, *58* (*1*), 63–70. DOI: https://doi.org/10.1016/0032-5910(89)80008-7

[11] G. H. Ganser, *Powder Technol.* **1993**, *77* (*2*), 143–152. DOI: https://doi.org/10.1016/0032-5910(93)80051-B

[12] A. Hölzer, M. Sommerfeld, *Powder Technol.* **2008**, *184* (*3*), 361–365. DOI: https://doi.org/10.1016/j.powtec.2007.08.021

[13] E. E. Michaelides, *J. Fluids Eng.* **2003**, *125* (*2*), 209–238. DOI: https://doi.org/10.1115/1.1537258

[14] H. Faxén, *Ann. Phys.* **1922**, *373* (*10*), 89–119. DOI: https://doi.org/10.1002/andp.19223731003

[15] A. M. Fayon, J. Happel, *AIChE J.* **1960**, *6* (*1*), 55–58. DOI: https://doi.org/10.1002/aic.690060111

[16] Z.-G. Feng, E. E. Michaelides, *Int. J. Multiphase Flow* **2002**, *28* (*3*), 479–496. DOI: https://doi.org/10.1016/S0301-9322(01)00070-2

[17] J. Happel, H. Brenner, *Low Reynolds Number Hydrodynamics: With Special Applications to Particulate Media*, 1. ed., 5. print ed., Noordhoff, Leyden **1991**.

[18] S. Whitaker, *AIChE J.* **1972**, *18* (*2*), 361–371. DOI: https://doi.org/10.1002/aic.690180219

[19] V. Gnielinski, *Forsch. Ingenieurwes.* **1975**, *41* (*5*), 145–153. DOI: https://doi.org/10.1007/bf02560793

[20] E. M. Sparrow, J. P. Abraham, J. C. Tong, *Int. J. Heat Mass Transfer* **2004**, *47* (*24*), 5285–5296. DOI: https://doi.org/10.1016/j.ijheatmasstransfer.2004.06.024

[21] M. M. Zdravkovich, *Flow Around Circular Cylinders*, Vol. *2*, Oxford University Press, Oxford **2003**.

[22] S. D. Dhole, R. P. Chhabra, V. Eswaran, *Int. J. Heat Mass Transfer* **2006**, *49* (*5–6*), 984–994. DOI: https://doi.org/10.1016/j.ijheatmasstransfer.2005.09.010

[23] A. G. Dixon, M. Ertan Taskin, M. Nijemeisland, E. H. Stitt, *Comput. Chem. Eng.* **2011**, *35* (*7*), 1171–1185. DOI: https://doi.org/10.1016/j.compchemeng.2010.12.006

[24] A. G. Dixon, *Chem. Eng. Res. Des.* **2014**, *92* (*7*), 1279–1295. DOI: https://doi.org/10.1016/j.cherd.2013.11.018

[25] *An Introduction to Computational Fluid Dynamics - The Finite Volume Method*, 2nd ed. (Eds.: H. K. Versteeg, W. Malalasekera), Pearson Education Limited, Essex **2007**.

[26] T.-H. Shih, W. W. Liou, A. Shabbir, Z. Yang, J. Zhu, *Comput. Fluids* **1995**, *24* (*3*), 227–238. DOI: https://doi.org/10.1016/0045-7930(94)00032-t

[27] M. Wolfshtein, *Int. J. Heat Mass Transfer* **1969**, *12* (*3*), 301–318. DOI: https://doi.org/10.1016/0017-9310(69)90012-x

[28] *Boundary-Layer Theory*, 9th ed. (Eds.: H. Schlichting, K. Gersten), Springer-Verlag, Berlin **2017**.

[29] P. J. Roache, *AIAA J.* **1998**, *36* (*5*), 696–702. DOI: https://doi.org/10.2514/2.457

[30] E. M. Moghaddam, E. A. Foumeny, A. I. Stankiewicz, J. T. Padding, *Chem. Eng. J.* **2021**, *407*, 127994. DOI: https://doi.org/10.1016/j.cej.2020.127994